Observation of charge transfer induced large enhancement of magnetic moment in a structurally disordered inverse Heusler alloy Fe_2RuGe

Sudip Chakraborty,[1,2] Shuvankar Gupta,[1,2] Vidha Bhasin,[3,2] Santanu Pakhira,[4] Céline Barreteau,[5] Jean-Claude Crivello,[5,6] Shambhu Nath Jha,[3] Dibyendu Bhattacharyya,[3] Maxim Avdeev,[7,8] Valérie Paul-Boncour,[5] Jean-Marc Greneche,[9] Eric Alleno,[5] and Chandan Mazumdar[1,2,*]

[1]*Condensed Matter Physics Division, Saha Institute of Nuclear Physics, 1/AF Bidhannagar, Kolkata 700064, India*
[2]*Homi Bhabha National Institute, Anushaktinagar, Mumbai 400094, India*
[3]*Atomic & Molecular Physics Division, Bhabha Atomic Research Centre, Mumbai 400 094, Maharashtra, India*
[4]*Ames National Laboratory, Iowa State University, Ames, Iowa 50011, USA*
[5]*Univ. Paris Est Creteil, CNRS, ICMPE, UMR 7182, 2 rue Henri Dunant, 94320 Thiais, France*
[6]*CNRS-Saint-Gobain-NIMS, IRL 3629, Laboratory for Innovative Key Materials and Structures (LINK), 1-1 Namiki, 305-0044 Tsukuba, Japan*
[7]*Australian Nuclear Science and Technology Organisation, Locked Bag 2001, Kirrawee DC, New South Wales 2232, Australia*
[8]*School of Chemistry, The University of Sydney, Sydney, New South Wales 2006, Australia*
[9]*Institut des Molécules et Matériaux du Mans, IMMM UMR CNRS 6283, Le Mans Cedex 9, 72085, France*

(Received 15 May 2023; revised 21 November 2023; accepted 1 December 2023; published 21 December 2023)

We report the successful synthesis of a new 4*d*-based polycrystalline inverse Heusler alloy Fe_2RuGe by an arc melting process and have studied in detail its structural, magnetic and transport properties complemented with first-principles calculations. X-ray and neutron diffraction, extended x-ray absorption fine structure, and ^{57}Fe Mössbauer spectroscopic studies confirm the single-phase nature of the system where the Fe and Ru atoms are randomly distributed in the 4*c* and 4*d* Wyckoff positions in a ratio close to 50:50. The formation of the disordered structure is also confirmed by the theoretical energy minimization calculation. Despite the random cross-site disorder of Fe and Ru atoms, magnetic measurements suggest not only a high Curie temperature of ∼860 K, but also a large saturation magnetic moment ∼4.9 μ_B per formula unit at 5 K, considerably exceeding the theoretical limit (4 μ_B per formula unit) predicted by the Slater-Pauling rule. Only a few Fe-based inverse Heusler alloys are known to exhibit such high Curie temperatures. Neutron diffraction analysis coupled with the isothermal magnetization value indicates that the magnetic moments in Fe_2RuGe are associated with Fe atoms only, which is also confirmed by Mössbauer spectrometry. Interestingly, in comparison to the cubic or hexagonal phase of the parent compound, Fe_3Ge, the Curie temperature of Fe_2RuGe has increased significantly despite the substitution of the nonmagnetic yet isoelectronic element Ru in this structurally disordered compound. Our theoretical calculation reveals that the large Fe moment (∼2.8 μ_B/Fe) on the 4*b* site can be attributed to a charge transfer from this Fe site towards its Ru neighbors while a significant moment (∼2 μ_B/Fe) is kept on the other Fe sites. Instead of expected Slater-Pauling value of 4 μ_B/f.u., the substantially increased observed total magnetic moment of ∼4.9 μ_B/f.u. is due to these electron charge transfers, which have not been previously reported in other ferromagnetic Heusler systems.

DOI: 10.1103/PhysRevB.108.245151

I. INTRODUCTION

Heusler alloys (HA) are known to be a series of enigmatic compounds that are often known to exhibit high ferromagnetic transition temperatures, even when all individual constituents are nonmagnetic [1,2]. HAs have a general chemical formula of X_2YZ, where X and Y are transition metal atoms and Z is generally a main group element atom. They crystallize in the Cu_2MnAl-type or $L2_1$-type structure ($Fm\bar{3}m$). Most HAs are highly ordered cubic intermetallic compounds with three crystallographic positions in their crystal lattice, viz. 4*a* (0,0,0), 4*b* ($\frac{1}{2}$, $\frac{1}{2}$, $\frac{1}{2}$), and 8*c* ($\frac{1}{4}$, $\frac{1}{4}$, $\frac{1}{4}$) [1]. It is generally seen that the occupancy of an atom at a particular site is determined by its number of valence electrons. Those with more valence electrons (X) tend to occupy the 4*c* and 4*d* positions, while atoms with fewer valence electrons (Y) tend to occupy the 4*b* position, which is generally known as the valence electron number rule [3]. However, there is also a subclass of HAs, where Y and one of the X atoms interchange their occupancy, and such systems are known as inverse HA, forming in the XA-type structure, also known as the Hg_2CuTi structure [4,5]. This latter crystallizes in $F\bar{4}3m$ space group with a splitting of 8*c* sites from $Fm\bar{3}m$ into two individual 4*c* and 4*d* sites. Another fascinating feature of HA system is the structural tunability, as many different combinations of 3*d*, 4*d*, and 5*d* transition metal elements can be used in the X and Y positions. Interestingly, one may realize that the choice of constituent

*chandan.mazumdar@saha.ac.in

elements and their occupancies determines the electronic band structure, which in turn controls most of the physical properties of these materials. As a result, HAs remain a very attractive system for appropriate crystal engineering [6–9].

The high Curie temperature and large saturation magnetic moment displayed by Heusler alloys recently got renewed attention due to their multifunctional properties viz. half-metallic ferromagnetism (HMF) [10–12], magnetic shape memories [13,14], magnetic spin-valve effects [15], magnetic skyrmions [16,17], spin-gapless semiconductors [18,19], etc., as all these properties could be used in a large number of technological devices operated at room temperature. For example, spintronics devices are considered to have huge advantages over conventional electronic devices due to their high speed for data processing, nonvolatile nature, and reduced power consumption rate [20]. It is generally seen that HA with the combination of both Co and Fe is particularly good for obtaining a high magnetic moment and elevated Curie temperature. A substantial number of Co-based systems are particularly known to exhibit HMF behavior and could be used for spintronic-related applications [11] [21]. On the other hand, although Fe-based HAs are rarely known to show such features, they have an enormous potential to be used as economically viable rare-earth free permanent magnet. In the quest for such new permanent magnetic material, the iron-rich compound, Fe_3Ge turns out to be one of the most remarkable systems [22]. The compound could be considered as the binary equivalent of Heusler alloy, where both the X and Y atoms are identical. Very interestingly, the compound is found to be stable at room temperature in two polymorphic crystal structures, viz., a cubic $L2_1$ phase (Cu_3Au type, $Pm\bar{3}m$, space group No. 221) formed by annealing at low temperatures ($<$ 1073 K) and a hexagonal DO_{19} phase (Mg_3Cd type, $P6_3/mmc$, space group No. 194) stabilized when the system is annealed at higher temperatures ($>$1073 K) [22]. Although both phases exhibit high Curie temperatures (655 K for the hexagonal phase and 755 K for the cubic phase) and large magnetic moments ($\sim 6\,\mu_B$/f.u.) at room temperature, the anisotropic magnetic properties of the hexagonal phase have generated considerable interest in its use as a permanent magnet. A lot of attempts have been made to modify the magnetic anisotropy by partially replacing Fe atoms with other 3d elements, viz., V, Cr, Mn, Co, and Ni [4,23–25]. It has been found that depending on the use of heavier or lighter 3d element substitution, the structural as well as magnetic properties can vary widely. Both Fe_2CoGe and Fe_2NiGe form in cubic inverse Heusler alloy structure [4], while $Fe_{3-x}Cr_xGe$ ($x < 0.70$) and Fe_2MnGe retain the hexagonal crystal structure [24,25]. $Fe_{3-x}V_xGe$ remains hexagonal for $x < 0.125$, but changes to cubic for $0.125 < x < 0.75$ [23]. The ferromagnetic Curie temperature for Fe_2CoGe ($T_C = 925$ K) and Fe_2NiGe ($T_C = 760$ K) is also higher than that of both the hexagonal as well as cubic phases of the parent compound, Fe_3Ge. In addition, although Co and Ni are considered magnetic elements, the magnetic moment is confined only to Fe in Fe_2NiGe, while both Fe and Co carry magnetic moment in Fe_2CoGe. On the other hand, the Curie temperature decreases in case of substitution by 3d elements lighter than Fe [4,23–25].

In light of such contrasting magnetic properties of $Fe_{3-x}T_xGe$ depending on the electronic configuration of 3d T element, it would be interesting to understand the role of the valence electron and the electronic band structure in this system. The substitution of isoelectronic elements belonging to the 4d (Ru) or 5d (Os) series would be highly helpful, despite the fact that both are nonmagnetic and isoelectronic to Fe, and are also susceptible to structural disorder. In this work, we report the successful synthesis of a new inverse Heusler alloy Fe_2RuGe and explored its structural and physical properties through different experimental and theoretical techniques. Two different spectroscopic techniques, viz., ^{57}Fe Mössbauer spectrometry and extended x-ray absorption fine structure (EXAFS) have been adopted to investigate the local structural disorders, while neutron diffraction studies have been carried out to investigate the magnetic spin arrangements. The electronic band structure calculation is also presented to complement the experimental results.

II. METHODS

A. Experimental details

The Fe_2RuGe polycrystalline ingot was prepared by the standard arc melting method in argon atmosphere on water-cooled Cu hearth. A stoichiometric amount of Fe chunk ($>$99.9%), Ru powder ($>$99.9%), and Ge lump ($>$99.999%) were used as starting materials. All the elements were melted and remelted together for five times after flipping each time to improve homogeneity. A negligible amount ($<$0.6%) of weight loss was recorded after the melting process. X-ray diffraction (XRD) measurement at room temperature was carried out using a commercial diffractometer (rotating Cu anode, 9 kW, Model: TTRAX-III, Rigaku Corp., Japan). The single-phase nature of the as-cast sample was confirmed by Rietveld refinement using FULLPROF software [26]. Microstructural analysis and compositional homogeneity were further investigated using a wavelength dispersive electron probe microanalysis (EPMA) spectrometer [Model: SX 100, Cameca, France].

Extended x-ray absorption fine structure (EXAFS) experiments on Fe_2RuGe were carried out at the Indus-2 Synchrotron Source (2.5 GeV, 100 mA) at the Energy-Scanning EXAFS beam line (BL-9) at Raja Ramanna Centre for Advanced Technology (RRCAT), Indore, India, which operates in the energy range of 4–25 keV. Both transmission and fluorescent modes can be used to perform EXAFS measurements in this beam line. A Rh/Pt-coated collimating meridional cylindrical mirror is used and the collimated beam is reflected by a mirror that is monochromatized by a double crystal monochromator (DCM) of Si(111) ($2d = 6.2709$ Å). For horizontal focusing, a sagittal cylinder (the second crystal of DCM) is used, and for vertical focusing of the beam, a Rh/Pt-coated bendable post mirror facing down at the sample position is employed. The higher harmonics content of the x-ray beam is rejected by detuning the second crystal of DCM. For EXAFS measurements, we have used the fluorescence mode. In this method, the incident x-ray beam angle is 45 degrees to the sample position, and a fluorescence detector, positioned at 90 degrees to the incident x-ray beam, is used to collect the signal. To measure the incident flux (I_0), an ionization chamber detector is placed before the sample,

and fluorescence intensity (I_f) is measured by a fluorescence detector. The relation, $\mu = (I_f/I_0)$, is used to calculate the x-ray absorption coefficient of the sample. The spectrum (as a function of energy) was acquired by scanning the monochromator over a particular range. In order to extract qualitative information about the local structure, the oscillations of the normalized absorption spectra [$\mu(E)$ vs. E] were transformed to absorption function $\chi(E)$ using the relation:

$$\chi(E) = \frac{\mu(E) - \mu_0(E)}{\Delta\mu_0(E_0)}. \tag{1}$$

Here, E_0 is the absorption edge energy, $\mu_0(E_0)$ is the background of exposed atom, and $\Delta\mu_0(E_0)$ is the step in $\mu(E)$ value at the absorption edge. The absorption coefficient as a function of energy $\chi(E)$, was changed to the absorption coefficient as a function of wave number $\chi(k)$ by the following equation,

$$k = \sqrt{\frac{2m(E - E_0)}{\hbar^2}}, \tag{2}$$

where, m is the mass of the electron. To intensify the oscillation at high $\chi(k)$, it is multiplied by k^2 and then to obtain the $\chi(R)$ vs. R plots, a Fourier transformation of $\chi(k)k^2$ functions into R space, regarding to the real distances calculated from the center of the absorbing atom, is done. The set of EXAFS data was analyzed by the program available in the DEMETER software package. Background reduction, Fourier transformation of the absorption spectra to derive $\chi(R)$ vs. R plots (using ATHENA code) [27], simulation of the theoretical plots from the assumed crystallographic structure, and finally the fitting of experimental data using the theoretically generated spectra (by ARTEMIS code) were also included in this package [27].

Isothermal magnetization measurements at low temperatures were performed in commercially available SQUID VSM (Quantum Design Inc., USA). Magnetic measurements in the temperature range 300–900 K were done in a high-temperature VSM equipped with an electromagnet (Model EV9, MicroSense, LLC Corp., USA).

Room-temperature, as well as high-temperature neutron diffraction experiments ($\lambda = 2.4395$ Å), were performed at ECHIDNA beam line in ANSTO, Sydney, Australia [28]. The details of the crystal structure as well as the analysis of the magnetic structure were performed by Rietveld refinement of neutron diffraction data using the FULLPROF software.

^{57}Fe transmission Mössbauer spectrometry was used to study the hyperfine structure at Fe sites. The spectra were obtained at 300 K and 77 K in a bath cryostat and using an electromagnetic transducer with a triangular velocity nature and a ^{57}Co source in a Rh matrix. The sample consists of a thin powdered and homogeneous layer containing about 5 mg-Fe/cm^2. The least-squares fitting method, which assumes quadrupolar doublets and/or magnetic sextets involving Lorentzian lines, has been applied to model the hyperfine structures using the MOSFIT program. The refined isomer shift values are corrected to that of α-Fe at 300 K, and an α-Fe standard was used to calibrate the velocity. Resistivity experiments using a standard four-probe method were performed in the temperature range 2–300 K using a PPMS Evercool-II instrument, (Quantum Design Inc., USA).

B. Computational methods

For the modeling part, the $L2_1$, inverse XA and disordered structures of Heusler alloys have been described in the same $F\bar{4}3m$ space group having both 4c and 4d positions (splitting of 8c site in $Fm\bar{3}m$), for a fuller discussion of site comparison. The calculations of enthalpy of formation, electronic structure, and spin polarization at 0 K were carried out using density functional theory (DFT). They were conducted using the projector augmented wave (PAW) method [29] implemented in the Vienna *ab initio* simulation package (VASP) [30,31]. The exchange correlation was described by the generalized gradient approximation modified by Perdew, Burke, and Ernzerhof (GGA-PBE) [32]. Energy bands up to a cutoff of $E = 600$ eV were used in all calculations and the convergence tolerance for the calculations was selected as a difference on the total energy within 1 $\times 10^{-6}$ eV/atom. For each structure, volume and ionic (for disordered compounds) relaxation steps were performed and the tetrahedron method with Blöchl correction [33] was applied. Spin-polarization calculations were considered for all the structures. In order to statistically simulate the chemical disorder in Fe_2RuGe, unit cells based on the concept of special quasirandom structure (SQS) [34] were generated for different possible disorder schemes. To generate the SQS, the cluster expansion formalism for multicomponent and multisublattice systems [35] was used as implemented in the Monte Carlo (MCSQS) code contained in the Alloy-Theoretic Automated Toolkit (ATAT) [36,37]. Subsequent DFT calculations were performed in order to test the quality of the SQS and to see how reliable the DFT results are. The root mean square (rms) error on correlation functions was used as another quality criterion in addition to the calculations including a different order of interactions. The rms error describes the deviation of the correlation function of the SQS (Π^k_{SQS}) from the correlation function of a fully random structure (Π^k_{md}) for all clusters k.

$$\mathrm{rms} = \sqrt{\sum_k \left(\Pi^k_{\mathrm{SQS}} - \Pi^k_{md}\right)^2}. \tag{3}$$

Several tests on the dependence of the type and number of clusters were performed to generate the disordered structure: Ge at 4a (0,0,0), Fe at 4b ($\frac{1}{2}$, $\frac{1}{2}$, $\frac{1}{2}$) and Fe = 0.5/Ru = 0.5 at 4c ($\frac{1}{4}$, $\frac{1}{4}$, $\frac{1}{4}$) and Fe = 0.5 and Ru = 0.5 at 4d ($\frac{3}{4}$, $\frac{3}{4}$, $\frac{3}{4}$). Finally, seven pairs, five triplets, and 11 quadruplets interactions were considered to obtain reliable results. Using these parameters, a disordered quaternary SQS cell of 28 atoms was generated.

III. RESULTS AND DISCUSSIONS

A. Structural characterization

The powder XRD data taken at room temperature is presented in Fig. 1. With the exception of very few small peaks (<2% of main peak intensity), all the peaks in the XRD pattern can be well indexed with a Hg_2CuTi-type (space group $F\bar{4}3m$, No. 216) inverse Heusler (XA-type) crystal structure with lattice parameter $a = 5.871(4)$ Å. It may be noted that Heusler alloys are prone to structural disorder, and despite the formation in cubic structure, such atomic disorders are known

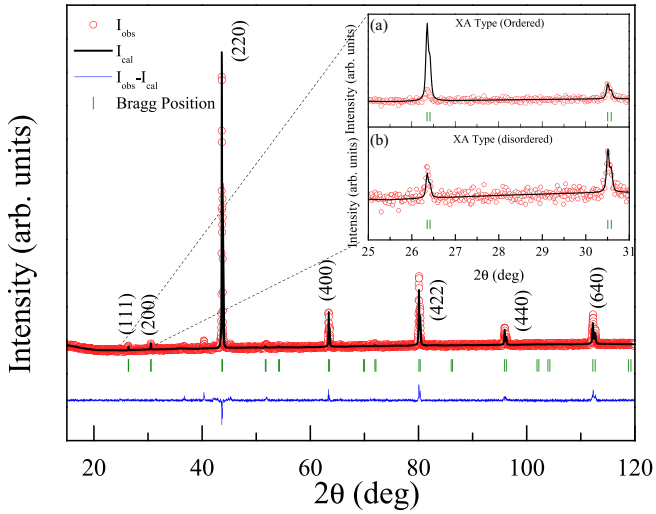

FIG. 1. Room-temperature powder XRD data along with Rietveld refinement. Insets (a) and (b) display enlarged views of superlattice reflection peaks fitted by ordered and disordered models, respectively.

to affect the intensity of the (111) and (200) superlattice Bragg peaks in the XRD patterns. For example, in $A2$-type disorder (all atoms mixed on a single site), both (111) and (200) peaks are absent, while in $B2$-type disorder (atoms mixed on two sites), only the (200) peak is present [3,12,38]. The occurrence of both (111) and (200) lines in Fig. 2 allows discarding $B2$ or $A2$ type of disorder. Our attempt to describe the crystal structure with an ordered variant (Ge occupy 4a position, Fe at 4b, Fe at 4c and Ru in 4d site) strongly undermined the experimentally observed (111) peak intensity (Fig. 1, inset), suggesting a disordered structure of different variant. Accordingly, we tried various combinations of site disorders and obtained the best result by considering a 50% permutation between Fe and Ru in the tetrahedral 4c and 4d sites (Fig. 2).

The Rietveld analysis, considering the above model, can fit the XRD pattern quite well (Fig. 1). The trace amount of the minority phase turns out to be that of $FeGe_2$ of less than 2% of the weight fraction of the primary phase. The structural disorder is further confirmed by the EXAFS and neutron diffraction data analysis, which will be discussed in later sections. This result is also in conformity with the theoretical calculations establishing that the disordered XA structure is more stable than the ordered one.

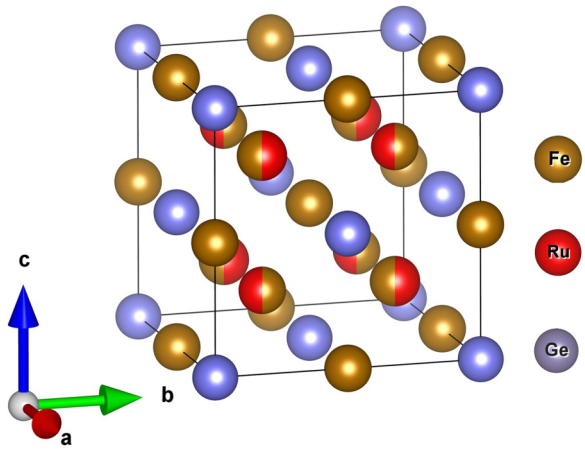

FIG. 2. Crystal structure of Fe_2RuGe in disordered form in $F\bar{4}3m$, mixing 4c and 4d sites with a 50:50 composition.

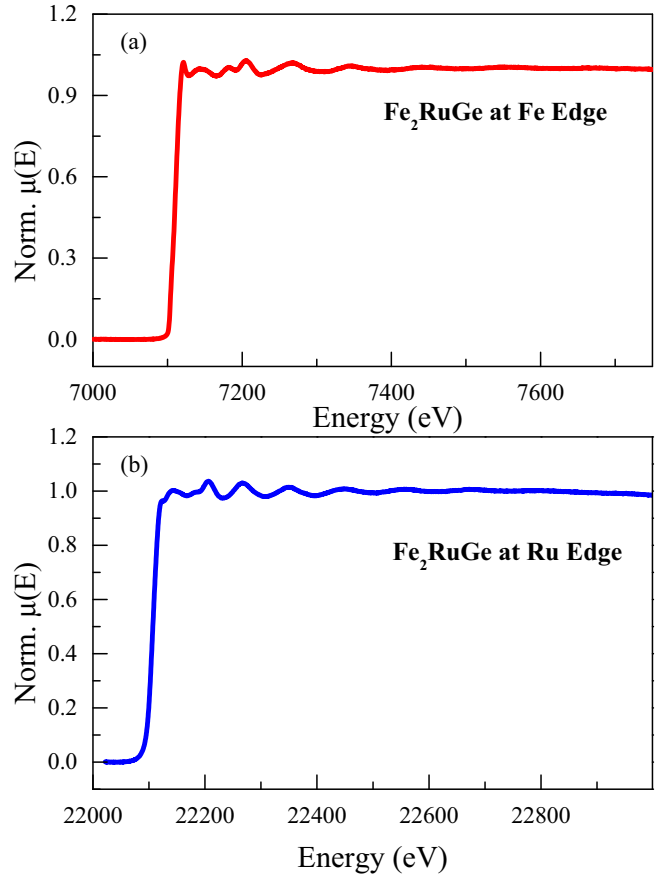

FIG. 3. Normalized EXAFS spectra of Fe_2RuGe taken at (a) Fe edge (b) Ru edge.

B. EXAFS analysis

The normalized EXAFS [$\mu(E)$ vs. E] spectra of Fe_2RuGe at the Fe and Ru edges, following the treatment presented in Eq. (1) and Eq. (7), are shown in Fig. 3. The $\chi(R)$ vs. R plots (Fourier-transformed EXAFS spectra) generated by the crystallographic information and the EXAFS equation of the Fe and Ru edge are shown in Fig. 4. Simultaneous fitting with several edges of various data sets is used in this approach. The $\chi(R)$ vs. R plots calculated at the Ru and Fe edges are fitted at the same time with common fitting parameters. The statistical significance of the fitting is improved by reducing the number of independent parameters below the Nyquist criterion. The value of R_{factor} was used to determine the goodness of fit, which is calculated by:

$$R_{\text{factor}} = \frac{[\text{Im}(\chi_{\text{dat}}(r_i) - \chi_{\text{th}}(r_i)]^2 + [\text{Re}((\chi_{\text{dat}}(r_i) - \chi_{\text{th}}(r_i)]^2]^2}{[\text{Im}(\chi_{\text{dat}}(r_i)^2] + [\text{Re}(\chi_{\text{dat}}(r_i)^2]}, \tag{4}$$

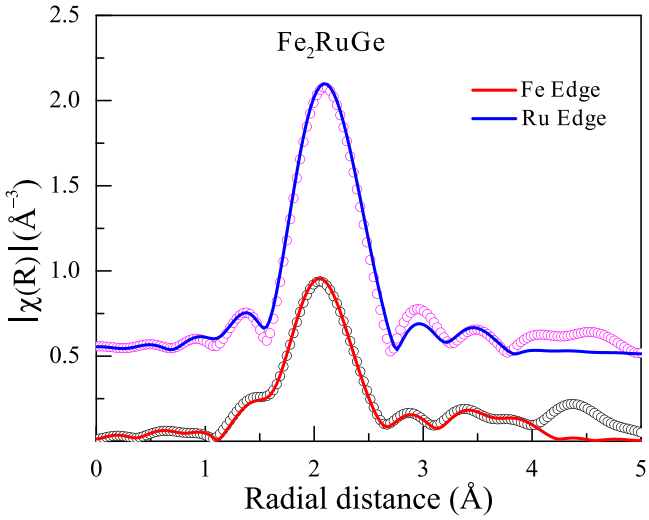

FIG. 4. Normalized and Fourier-transformed EXAFS spectra of Fe_2RuGe taken at Fe edge (top panel) and Ru edge (bottom panel), respectively.

where χ_{th} and χ_{dat} are the theoretical and experimental χ_R values, respectively. Re and Im are the real and imaginary components of the respective quantities. To theoretically simulate the EXAFS spectra of Fe_2RuGe, the structural information (lattice parameters and nearest-neighbor numbers) have been taken from the XRD results. The atomic distances (R), coordination numbers (N), and disorder (Debye-Waller) factors (σ^2), which give the mean-square variations of the distances, were used as fitting parameters. The fitting was done up to 4 Å. A simultaneous fitting of the Ru and Fe edges could be obtained for the disordered structure only. The refined values of the parameters are listed in Table I.

From the fitting of Fe edge of the Fourier transformed spectra, we found that the main peak near 2 Å has a contribution from all Fe-Fe (2.48 Å), Fe-Ru (2.53 Å), and Fe-Ge (2.48 Å) distances. The second intense peak near 3 Å arises due to the contribution of Fe-Ru (2.89 Å) and Fe-Fe (2.89 Å) and the peak near 4 Å consists of the contribution of Fe-Fe (4.07 Å) and Fe-Ru (4.17 Å). From the coordination number and bond length analysis, we found occupancy of the 4*b*, 4*c*, and 4*d* sites between Fe and Ru is nearly 71%:29%, close to 66%:33%. Similarly, we analyzed the Ru-edge Fourier transformed spectra, where the main peak near 2 Å arises due to the contribution of scattering paths of Ru-Ge (2.53 Å) and Ru-Ru (2.53 Å). The second peak consists of the scattering paths of Ru-Ru (2.88 Å) and Ru-Fe (2.88 Å) and the third peak near 4 Å consists of Ru-Fe (4.07 Å) and Ru-Ru (4.07 Å). From these data we also calculated the intermixing between 4*c* and 4*d* sites to be 58:42. This data is consistent with the Fe edge data also. From the XRD analysis in Sec. III A we found that the disorder between Fe and Ru in 4*c* and 4*d* sites is about 50:50. Our EXAFS analysis is also in agreement with this.

C. dc magnetization study

To measure the magnetic ordering temperature and magnetic moment of Fe_2RuGe, the magnetization as a function of temperature as well as magnetic field was measured. The isothermal magnetic measurements at room temperature show a soft ferromagnetic character with a rather large magnetic moment (~4.71 μ_B/f.u.) (Fig. 5), suggesting ferromagnetic ordering at a temperature above 300 K. Accordingly, we performed magnetic susceptibility measurements in a VSM with electromagnet in the temperature range 300–900 K under a magnetic field of 100 Oe. Very interestingly, the system exhibits ferromagnetic ordering at ~860 K (estimated from dM/dT curve) (Fig. 6, inset), much higher than its binary parent compound, Fe_3Ge (T_C = 755 K) [22]. It may be noted here that the minor phase of $FeGe_2$ detected from our XRD analysis are known to exhibit a ferromagnetic ordering at a much lower temperature, ~290 K [39], and hence the observed ordering at ~860 K must arise from the main phase. The large magnetic moment in the isothermal magnetic measurement at 300 K also confirms the ferromagnetic ordering of the primary phase, Fe_2RuGe. Substituting a magnetic Fe atom with a nonmagnetic Ru atom, having a random mixed site occupancy increases T_C even in comparison to the case where 3*d* atoms such as V, Cr, Mn, and Ni are substituted [4,23–

TABLE I. Extracted values of Bond length (R), coordination number (N), and Debye-Waller or disorder factor σ^2 obtained from EXAFS fitting for Fe_2RuGe at Fe and Ru edge.

Fe edge				Ru edge			
Path	R (Å)	N	σ^2	Path	R (Å)	N	σ^2
Fe-Ru	2.53 ± 0.01	4	0.0250 ±0.0023	Ru-Ge	2.53 ± 0.01	4	0.0082 ±0.0003
Fe-Fe	2.48 ± 0.01	4	0.0164 ±0.0004	Ru-Fe	2.53 ± 0.01	4	0.0082 ±0.0003
Fe-Ge	2.48 ± 0.01	3	0.0164 ±0.0004	Ru-Ru	2.88 ± 0.01	2.3	0.0073 ±0.0014
Fe-Ru	2.89 ± 0.01	1.7	0.0034 ±0.0004	Ru-Fe	2.88 ± 0.01	3.7	0.0073 ±0.0014
Fe-Fe	2.88 ± 0.01	4.3	0.0080 ±0.0004	Ru-Ru	4.07 ± 0.03	5.1	0.0075 ±0.0047
Fe-Ge	3.11 ± 0.01	6	0.0247 ±0.0017	Ru-Fe	4.07 ± 0.03	6.9	0.0075 ±0.0047

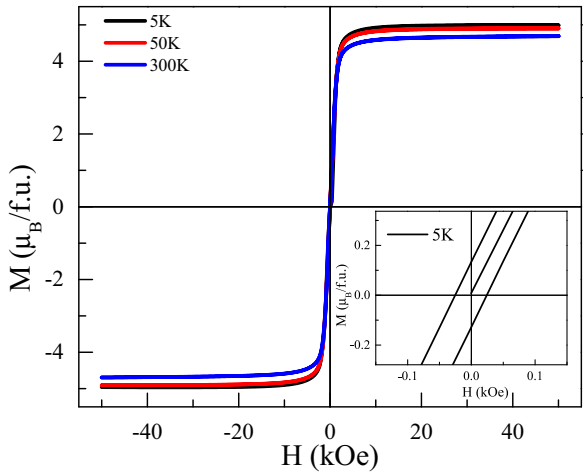

FIG. 5. Isothermal magnetization plot at various temperatures. Inset represents the hysteresis phenomenon at $T = 5$ K.

25]. The isothermal magnetic measurement was also extended to lower temperatures to compare it to the theoretically estimated moments. The data taken at 5, 50, and 300 K are shown in Fig. 5. Even at the lowest measured temperature, 5 K, the coercive field retains its soft magnetic character ($H_C = 130$ Oe), and the saturation moment is only slightly enhanced to ~4.92 μ_B/f.u.. It may be pointed out here that the well-known Slater-Pauling (S-P) rule provides a theoretical limit of the magnetic moments in Heusler alloy systems. According to the S-P rule, the saturation magnetic moment (M) can be expressed as (N_V −24) μ_B/f.u. where N_V is the valence electron number [1]. The atomic disorder present in the system is known to reduce the experimental value in comparison to the S-P-rule prediction [12]. Since Fe and Ru are randomly distributed in 4*c* and 4*d* positions in Fe_2RuGe, one thus expects a considerably diminished value of magnetic moment. Surprisingly, the experimentally observed saturation magnetic moment (~4.92 μ_B/f.u.) for Fe_2RuGe is found to

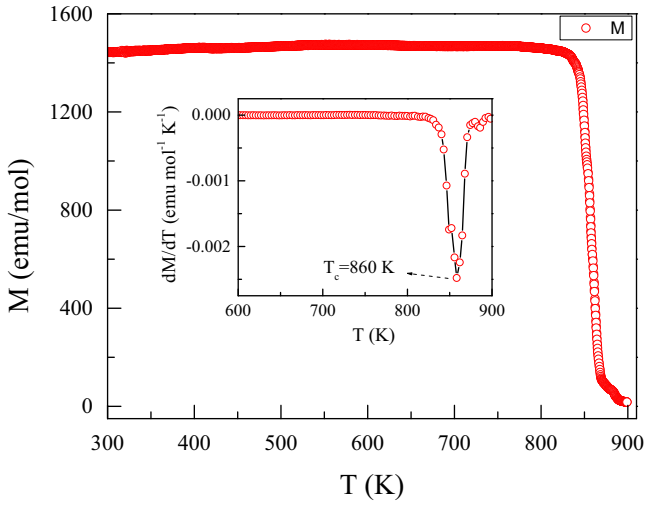

FIG. 6. Magnetization *vs*. Temperature plot in 100 Oe applied magnetic field. Inset shows the first derivative of magnetization as a function of temperature.

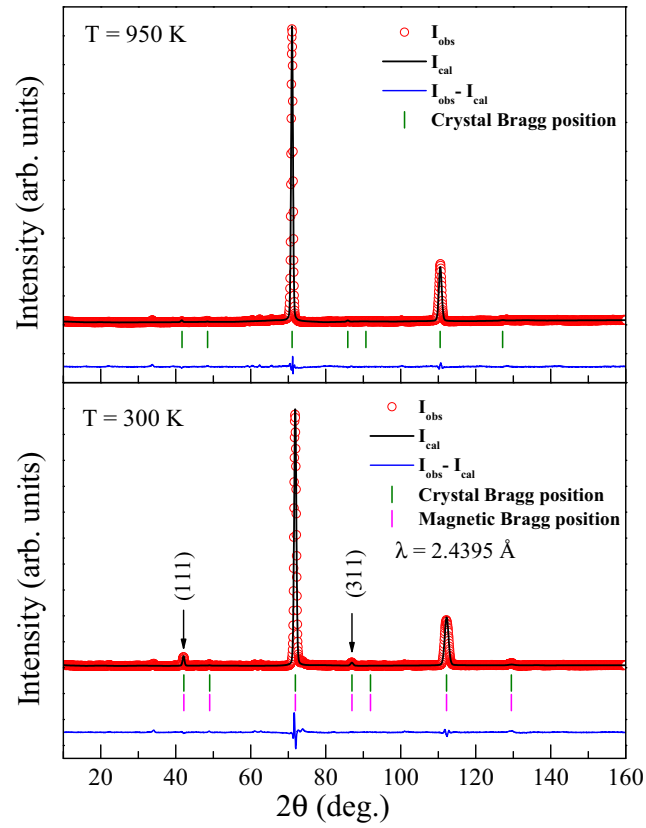

FIG. 7. Neutron diffraction pattern along with full Rietveld refinement of paramagnetic (top panel) and magnetically ordered temperature (bottom panel).

be much higher than that theoretically predicted (4 μ_B/f.u.). Although a few Fe-based HA are already known to exhibit saturation moment higher than that predicted by the SP rule [4], Fe_2RuGe occupies a special place because it exhibits such a large value despite its inherent atomic disorder involving the moment carrying Fe atoms. As up to now most studied HMF systems obey the S-P rule [12], the specific behavior of Fe_2RuGe needs other experimental measurements (neutron diffraction and Mössbauer spectrometry) as well as theoretical calculations to be more clearly understood.

D. Neutron diffraction

Neutron powder diffraction measurements have been carried out on Fe_2RuGe at 300 K and 950 K, respectively, below and above its Curie temperature ($T_C \sim 860$ K) to analyze the nuclear structure at 950 K and the long-range magnetic order at 300 K (Fig. 7). The diffraction pattern at 950 K, i.e., in the paramagnetic region, can be well refined in the cubic space group $F\bar{4}3m$ with lattice parameter as $a = 5.936(2)$ Å, while the Fe and Ru occupy the 4*c* and 4*d* positions with occupation rates of 55% and 45%, respectively. This agrees with the XRD data analysis described earlier in Sec. III A and confirms the larger stability of the disordered XA structure compared to Heusler or ordered XA structure. We may, however, note that the intensity of (111) and (200) Bragg peaks, which are generally considered as a signature of perfect crystalline ordering, have much-reduced intensity in the ND spectra in comparison

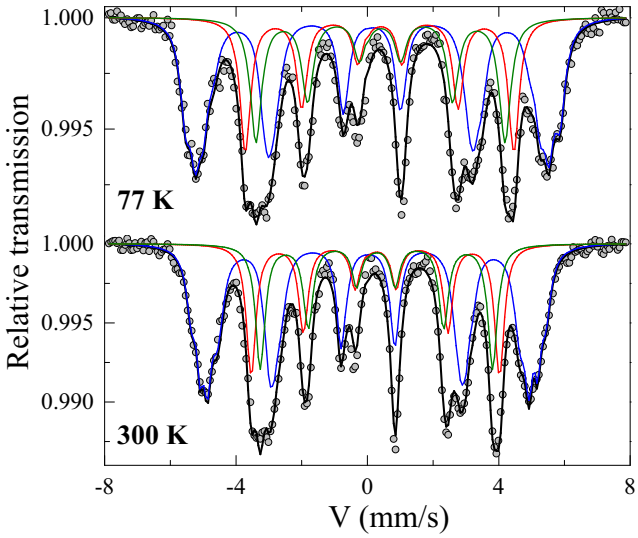

FIG. 8. ^{57}Fe Mössbauer spectra of Fe_2RuGe taken at 300 K (bottom panel) and at 77 K (top panel), respectively.

to XRD data, which can be explained due to the different atomic scattering factors of neutron and x-ray. The small peak at $2\theta = 33.9°$ can be refined with 0.6% of $FeGe_2$ impurity. The NPD pattern measured at 300 K, in the magnetically ordered state, appears to be nearly like that at 950 K, except for a moderate increase in the intensity of the (111) and (311) crystal Bragg peaks. Assuming the structural model refined in the paramagnetic region (950 K) remains similar at 300 K, the absence of additional peaks beyond the allowed crystal Bragg positions ruled out the antiferromagnetic type of order in this system. Rietveld refinement of the 300 K data yields a refined cell parameter $a = 5.8787(2)$ Å close to the XRD value. A good refinement was obtained assuming a ferromagnetic alignment of the Fe sublattice in agreement with the magnetization data. In a powder pattern, all the axes are equivalent to a cubic structure, and it is not possible to specify a preferred orientation of the magnetic moments. Since the intensity of only a few Bragg peaks is related to magnetic ordering, with a small intensity compared to the nuclear contribution, it was not possible to refine independently each Fe moment without a divergence of the fit. A unique Fe moment was therefore assumed for all sites (i.e., 4*b*, 4*c,* and 4*d*) and the refinement of the Fe moment intensity lead to 2.49(4) μ_B/Fe or 4.98 μ_B/f.u. ($RB_{nucl} = 0.65\%$ and $R_{Mag} = 7.78\%$). This value agrees quite well with the isothermal magnetization measurements (Sec. III C) with $M = 4.69$ μ_B/f.u. at 300 K and $M = 4.92$ μ_B/f.u. at 5 K. In order to check if a Ru magnetic contribution had to be taken into account, a fit was performed by fixing the values of Fe and Ru moment to the values calculated by DFT: M(Fe-4*b*) = 2.74 μ_B/Fe, M(Fe-4*d*) = 1.92 μ_B/Fe, and M(Ru) = 0.33 μ_B/Ru (See Sec. III F). This leads to higher values of the refinements factors (RB_{nucl} = 1.25% and R_{Mag} = 15%). To conclude this part, we consider that the larger total Fe moment in the *X*A ordered or disordered structure is related to the Fe:Ru 4*b* charge transfer.

E. ^{57}Fe Mössbauer spectrometry

As the analysis of the Fe_2RuGe ND spectra does not allow the determination of site-specific Fe moments, ^{57}Fe Mössbauer spectrometry was used to check the relative population of Fe atoms and their respective magnetic moments (determined appropriately from the magnetic hyperfine fields of the individual components) in the three crystallographic positions, namely 4*b*, 4*c*, and 4*d*. The Mössbauer spectra taken at 300 K and 77 K (shown in Fig. 8) are quite similar and show complex magnetic structures consisting of well-resolved magnetic hyperfine structures with broadened and asymmetrical lines. Initial inspection of the spectra reveals that the outermost lines belong to the major magnetic sextet that must be described using a discrete distribution of hyperfine fields (ranging from about 270–340 kOe and 290–360 kOe at 300 and 77 K, respectively), common values of isomer shift and quadrupole shift (see the mathematical procedure discussed in Varret *et al.* [40] and Campbell *et al.* [41]). The rest of the hyperfine structure can be described by another, but narrower, distribution of hyperfine fields (from about 210–240 kOe and 230–270 kOe at 300 and 77K, respectively), common values of isomer shift and quadrupole shift. But the two values of isomer shift are different. Several models can be proposed to describe each spectrum: the first description consists therefore of two magnetic components with broad and Lorentzian lines characterized by two different values of isomer shift attributed to the two Fe 4*b* and 4*d* sites. The Fe, Ru, and Ge disorder explains why only two components are not able to describe perfectly the hyperfine structures observed at 300 and 77 K. Indeed, the second description for both spectra involve three magnetic components, by splitting the component with the lowest values of hyperfine fields into two components: each

TABLE II. Refined values of hyperfine parameters estimated from the Mössbauer spectra at 300 and 77 K: δ, 2ϵ, and B_{hf} correspond to the isomer shift, quadrupolar shift, and hyperfine field, respectively.

T (K)	Site	δ mm/s ± 0.01	2ϵ mm/s ± 0.01	B_{hf} kOe ± 0.5	ratio (%) ±1
300 K	Fe-4*b*	<0.17>	<0.01>	<306>	55
	Fe-4*c*	<0.39>	<−0.01>	<233>	23
	Fe-4*d*	<0.41>	<0.02>	<218>	22
		<0.28>	<0.01>	<269>	
77 K	Fe-4*b*	<0.28>	<−0.01>	<330>	52
	Fe-4*c*	<0.50>	<0.01>	<252>	24
	Fe-4*d*	<0.53>	<0.01>	<234>	24
		<0.40>	<0.01>	<288>	

TABLE III. Calculated enthalpy of formation $\Delta_f H$ and total magnetic moment for each ordered type of Fe_2RuGe, and one disordered case.

	4*a*	4*b*	4*c*	4*d*	$\Delta_f H$ (kJ/mol^{-1})	Magnetic Moment (μ_B/f.u.)
Heusler (Cu_2MnAl)	Ge	Ru	Fe	Fe	2.79	5.0
*X*A structure (Hg_2CuTi)	Ge	Fe	Ru	Fe	−18.94	5.0
Disordered *X*A structure	Ge	Fe	Fe:Ru	Fe:Ru	−20.24	4.9

results from the superposition of several magnetic sextets to describe the asymmetry and width of the lines, in order to take into account the disordered atomic environments. The corresponding refined mean values of the hyperfine parameters are listed in Table II.

The relative absorption areas are estimated at 55%, 23%, and 22% for the three sites Fe-4*b*, Fe-4*c*, and Fe-4*d*, respectively. Assuming the same values of their respective Lamb-Mössbauer factors, they directly give rise to the proportions of Fe atoms that match quite well with our analysis of ND and XRD patterns (Sec. III A, Sec. III D). Considering the fact the larger hyperfine field value corresponds to the 4*b* site in inverse Heusler alloys [4], the mean hyperfine field values at 300 K for the three magnetic components as 306 kOe, 233 kOe, and 218 kOe are assigned to 4*b*, 4*c*, and 4*d* sites, respectively. The individual Fe moments corresponding to the Wyckoff positions 4*b*, 4*c*, and 4*d* in Fe_2RuGe can be estimated from the three different hyperfine field components, provided that the magnetic hyperfine field values can be properly scaled with the respective magnetic moments. Usually, α-Fe with a magnetic moment of 2.2 μ_B yields a hyperfine field of ∼330 kOe, and most often this reference is used as the calibration factor. Using this approach, it was concluded in a previous study on the structurally similar compound $Fe_{3-x}Ru_xSi$ that Ru atoms contains a magnetic moment of about ∼1.3 μ_B for $x = 0.75$, while the proposed moment in Ru is slightly reduced to 1 μ_B in Fe_2RuSi [42]. This result is really surprising, as only a handful of materials are known where Ru carries magnetic moments [43]. If we implement the same calibration factor in Fe_2RuGe as well, and compare the result with isothermal magnetization data, we also would have to assign a magnetic moment of 0.7 μ_B on Ru atoms in our sample of Fe_2RuGe. However, the neutron diffraction experiment presented above ruled out the presence of any significant magnetic moment at the Ru site. In this context, we may like to point out that the relationship between the magnetic hyperfine field and the magnetic moment are not so straightforward as elaborated earlier in literature for many different Fe-containing DO_3-type alloys [44,45] as well as for other binary systems [46]. In some other Fe-based Heusler compounds too, it has also been suggested that a magnetic moment of 2.2 μ_B/Fe would correspond to 275 kOe [4]. Such a change is usually caused by the presence of a large anisotropic hyperfine field involving a dipolar field, a noncubic distribution of spin density in the iron atom, an anisotropic *g* factor, etc. [45]. For our calculation, we have

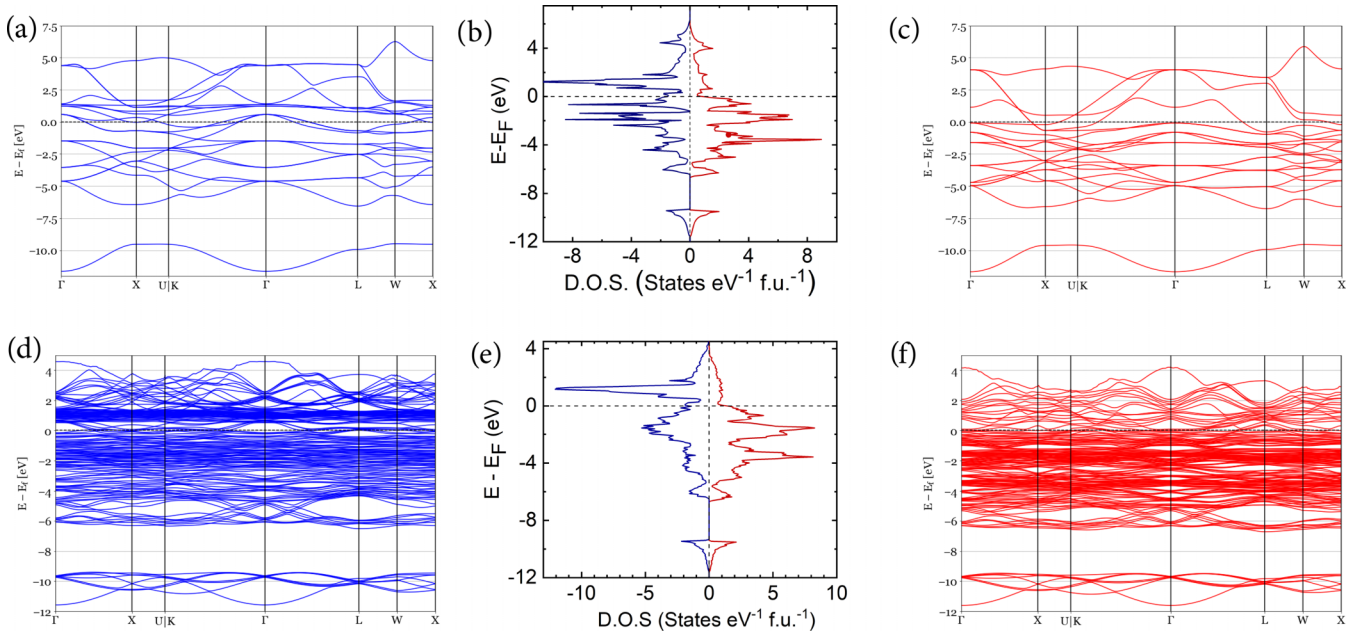

FIG. 9. Spin-polarized band structure and density of states of Fe_2RuGe in ordered Hg_2CuTi-type structure: (a) minority (spin-down) band (b) density of states, (c) majority (spin-up) band. Spin-polarized band structure and density of states of Fe_2RuGe in disordered Hg_2CuTi-type structure: (d) minority (spin-down) band (e) density of states, (f) majority (spin-up) band. The energy axis zero point has been set at the Fermi level and the spin-up (minority) and spin-down (majority) electrons are represented by positive and negative values of the DOS, respectively.

TABLE IV. Calculated magnetic moment for each ordered type of Fe_2RuGe, and one disordered case.

	4*a* (μ_B/f.u.)	4*b* (μ_B/f.u.)	4*c* (μ_B/f.u.)	4*d* (μ_B/f.u.)	*P* (%)
$L2_1$ (Cu_2MnAl)	Ge = −0.05	Ru = 1.3	Fe = 1.94	Fe = 1.94	−33.3%
*X*A (Hg_2CuTi)	Ge = −0.04	Fe = 2.76	Ru = 0.33	Fe = 1.92	−29.9%
Disordered *X*A	Ge = −0.04	Fe = 2.74	Fe:Ru with Ru = 0.16	Fe:Ru with Fe =1.98	−2.7%

thus utilized the reference of Fe_3Ge, which can be regarded as the parent compound of our studied Heusler system, Fe_2RuGe, where a magnetic hyperfine field value of 220 kOe had been associated with 2 μ_B/Fe atom [45]. If we use this calibration factor for Fe_2RuGe, we find the Fe magnetic moment values at 4*b*, 4*c*, and 4*d* sites as 2.78, 2.12, and 1.98 μ_B, respectively, giving a resulting magnetic moment of $<4.83>\mu_B$, that matches quite well with the isothermal magnetization measurement and theoretical calculations.

F. Theoretical analysis

In order to theoretically establish the most stable crystal structure, several crystal configurations were studied by DFT calculations. We considered the ordered Cu_2MnAl-type corresponding to the full Heusler structure ($L2_1$) and the Hg_2CuTi-type known as the *X*A structure. For both structures, the optimized crystal structure was obtained from DFT calculations and the enthalpies of formation are summarized in Table III. Our calculations show that the Cu_2MnAl-type structure is less stable than the *X*A structure, which is in good agreement with the structural analysis (Sec. III A). Moreover, a structural disorder of Fe and Ru on the 4*c* and 4*d* positions, in the *X*A structure, leads to a more stable compound, thus confirming the XRD, ND, and EXAFS data.

Figures 9(a)–9(c) show the calculated spin-polarized band structure and the calculated density of states (DOS) of the ordered *X*A structure. As it can be seen, the DOS shows no band gap at the Fermi level (E_F) for either the majority or minority spin population. This explains a rather low value of the spin polarization, with $P(X\text{A}) = \frac{DOS^{\uparrow}(E_F)-DOS^{\downarrow}(E_F)}{DOS^{\uparrow}(E_F)+DOS^{\downarrow}(E_F)} = -29.9\%$, and P(Heusler structure) $= -33.3\%$. As in many other Heusler compounds, the spin polarization drastically decreases when the disorder increases, *P* drops to −2.7% in the disordered *X*A inverse Fe_2RuGe too. As in Figs. 9(a)–9(c), Figs. 9(d)–9(f) shows the calculated spin-polarized band structure and the associated DOS of the disordered *X*A structures where no semiconducting behavior can be noticed because both spin directions correspond to a metallic ground state. The calculated total magnetic moment, for all configurations, is in good agreement with the experimental magnetic moment, always around 5 μ_B/f.u.. Although all calculated total magnetic moments are almost the same for the three configurations, only the ordered and disordered *X*A types show significant differences in atomic moment of Fe compared to the full Heusler configuration. It may be noted that the magnetic moment is shared between the Fe and Ru elements for the Heusler type. In contrast to this, in the *X*A structure type, the magnetic moment of the Ru element is considerably decreased whereas the magnetic moment carried by the Fe atom in 4*b* positions is strongly increased (Table IV).

In the full Heusler configuration, the Fe-8*c* site is surrounded by 4 Ge and 4 Ru atoms, while the nearest Fe neighbors are at a large distance and the mean Fe moment is 1.98 μ_B/Fe. In the ordered and disordered *X*A structures, it can be observed that Fe-4*b* atoms surrounded by 4 Fe and 4 Ru atoms have a enhanced moment close to 2.8 μ_B/Fe while Fe-4*c*(*d*) atoms surrounded by 4 Fe and 4 Ge atoms retain a moment close to 1.9 μ_B/Fe. The spin-polarized DOS projected on each site for the *X*A ordered structure clearly shows a different contribution of the Fe site to the spin-polarized DOS (Fig. 10), with a stronger interaction of Ru orbitals with Fe-4*b* than with Fe-4*c*. The calculation of the Bader charges, as shown in Table V, reveals a larger electronic charge transfer from Fe-4*b* (−0.35) to Ru-4*d* (+0.47) in the disordered *X*A structure compared to the direct structure, −0.13 to +0.26, for both Fe and Ru sites, respectively. In fact, the charge transfer from Fe-4*d* is less important in *X*A structure since its atomic environment is surrounded by Fe and Ge. Due to the charge transfer from Fe to Ru, the number of unpaired electrons for the Fe-4*b* atom increases, explaining the enhancement of its magnetic moment in comparison with Fe-4*d* and the low value for the Ru moment. Such charge transfer is also responsible for the enhancement of the magnetic moment of the Fe at 4*b* site, compared to the average moment on Fe in the parent compound Fe_3Ge.

The observed enhancement of magnetic moment (4.92 μ_B/f.u.) from the expected S-P value (4 μ_B/f.u.) in Fe_2RuGe (VEC 28) is indeed quite rare as among the known inverse HAs. Only a handful of such material are known to exists, primarily in Fe-based systems only. One such system is Fe_2CoGe (VEC 29) that exhibits a magnetic moment

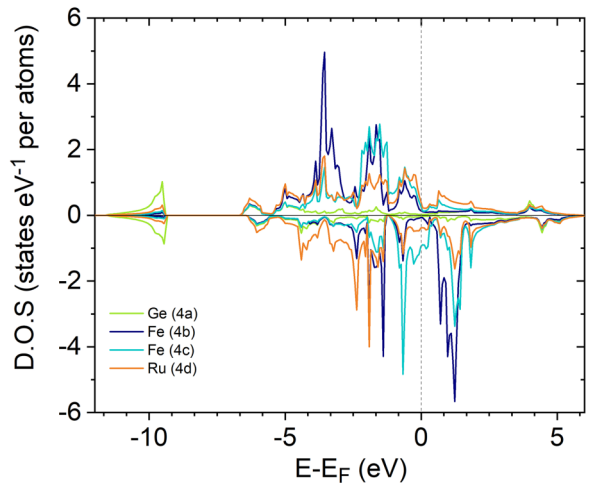

FIG. 10. Projected spin-polarized DOS on each site for the *X*A-ordered structure.

TABLE V. Bader charge transfer in Fe_2RuGe.

	4*a* (electron)	4*b* (electron)	4*c* (electron)	4*d* (electron)
Heusler (Cu_2MnAl)	Ge: +0.00	Ru: +0.26	Fe: −0.13	Fe: −0.13
*X*A structure (Hg_2CuTi)	Ge: −0.11	Fe: −0.35	Ru: +0.53	Fe: −0.06
Disordered *X*A structure	Ge: −0.07	Fe: −0.35	Ru: +0.47	Fe: −0.06

(5.40 μ_B/f.u.), instead of expected 5 μ_B/f.u. The enhancement of magnetic moment in Fe_2CoGe (0.40 μ_B) is also smaller than that observed in the present case of Fe_2RuGe (0.92 μ_B). Nevertheless, in order to make an enhanced comprehension of the distinction between Fe_2RuGe (VEC = 28) and Fe_2CoGe (VEC = 29), we have additionally carried out band structure computations for Fe_2CoGe within the identical disordered *X*A configuration. In this structure, only Fe is present in the 4*b* site, while Co (in place of Ru) and Fe share the same 4*c*:4*d* sites with a 50%:50% statistic occupation. The outcomes of these DFT computations for Fe_2CoGe are given in Table VI. First, we can compare the calculated values of magnetic moments, both overall and site specific, with the experimental values. While the experimental value is approximately 5.0 μ_B/f.u. in both compounds, the two types of total moment values calculated in the Ru and Co compounds, respectively, are in good agreement. As can be seen below, the computed site-specific Fe moments likewise agree very well with the experimental ones (in parentheses). M(Fe-4*b*) = 2.74 (2.78) μ_B/atom and M(Fe-4*c*:4*d*) = 1.98 (2.12) μ_B/atom are the values for Fe_2RuGe, while M(Fe-4*b*) = 2.67 (2.68) μ_B/atom and M(Fe-4*c*:4*d*) = 1.56 (1.51) μ_B/atom are the values for Fe_2CoGe. When comparing the computed Fe moments of Fe_2RuGe and Fe_2CoGe, it can be observed that the 4*b* site of both compounds has a greater Fe moment (∼2.7 μ_B/atom). A significant charge transfer of about −0.3 electrons per Fe atom is associated with this moment. Therefore, although the enhancement of larger Fe-4*b* moment is not unique to Fe_2RuGe, nevertheless the Fe atom at the 4*c*:4*d* site is actually what makes Fe_2RuGe special. Fe_2RuGe (VEC = 28) has a much larger moment of ∼2 μ_B/atom, while Fe_2CoGe (VEC = 29) has a moment of ∼1.5 μ_B/atom. The charge transfer that Fe-4*c*:4*d* experiences in the first compound is negative (−0.06), whereas in the second compound, it is positive (+0.03). While Co only receives +0.18 electrons and still bears 1 μ_B/atom, all of the Fe electrons in Fe_2RuGe are mostly transferred to Ru (+0.47), which is almost nonmagnetic. The positive Bader charge transfer of Ge (+0.06) in Fe_2CoGe compared to Fe_2RuGe (−0.07) is also likely to play a crucial role. Fe_2RuGe is therefore unique to this effect for Fe at the 4*c*:4*d* site, which helps explain why its total magnetic moment exceeds the S-P limit. In conclusion, we have discovered a novel effect in Fe_2RuGe and have successfully linked it to calculated charge transfer between the atoms that make up the material.

TABLE VI. Bader charge transfer in Fe_2CoGe (considering disordered *X*A-type structure).

Fe_2CoGe	4*a*	4*b*	4*c*:4*d*	4*d*:4*c*
Occupancy	Ge	Fe	Fe:Co	Fe:Co
Magnetic moment (μ_B/f.u.)	−0.05	2.67	Co: 1	Fe: 1.56
Total magnetic moment		5.18 (μ_B/f.u.)		
Bader Charge (electron)	+0.06	−0.27	+0.18	+0.03

G. Resistivity study

In Sec. III F, it is predicted that Fe_2RuGe has density of states in both up and down spin configuration at the Fermi level. To check its validity, we have performed resistivity experiments. Figure 11 represents the temperature-dependent electrical resistivity [$\rho(T)$] behavior of Fe_2RuGe measured in the absence of magnetic field (H = 0 kOe) in both heating and cooling cycles. We could not observe any irreversibility between these data: thus we ruled out any possibility of a structural transition in the system. In the case of a ferromagnetic material, the temperature dependence of electrical resistivity can be attributed to three different types of scattering factors. According to Matthiessen rule, all these contributions arise due to different types of factors such as (i) contribution due to scattering of conduction electrons by the lattice defects, ρ_0, (ii) phonon scattering, ρ_P, (iii) magnon scattering and electron-electron interaction, ρ_M, are additive in nature. From Fig. 11 we can see that the residual resistivity ratio (RRR) of Fe_2RuGe (ρ_{300K}/ρ_{5K}) is around 1.625, which clearly indicates the existence of substantial structural disorder in the sample [47,48]. We can say that resistivity of any ferromagnetic material is

$$\rho(T) = \rho_0 + \rho_P(T) + \rho_M(T). \tag{5}$$

The phonon scattering term can be written as [12,49]

$$\rho_P = C\left(\frac{T}{\Theta_D}\right)^5 \int_0^{\frac{\Theta_D}{T}} \frac{x^5}{(e^x-1)(1-e^{-x})} dx \tag{6}$$

and the magnon and electron contribution as BT^2. Here Θ_D is the Debye temperature and C is scattering constant [12]. As the T_C is quite high, we have fitted the data using Eq. (5) From the fitted parameters, phonon contribution was found much higher compared to the magnon contribution. However, Eq. (5) fits the data well within the region $60 < T < 300$ K only, but is unable to fit the low-temperature region properly. From the fitted results we get Θ_D = 360 K. Generally, electron-electron (e-e) and electron-magnon (e-m) lead to a quadratic temperature dependence of resistivity. However, between these two, the dominant contribution can be inferred from the magnitude of the coefficient, B. Normally, B is of the order of 10^{-2} nΩ cm K^2 for e-e interaction while it is normally two orders higher for e-m interaction. From the

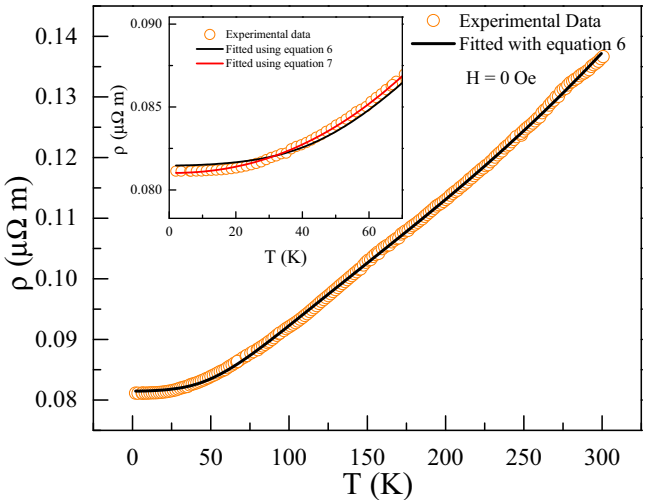

FIG. 11. Zero-field electrical resistivity measured at a function of temperature.

fitting, we got the value of B (e-e interaction coefficient) to be 4.57×10^{-5} $\mu\Omega$ cm K^2, which falls within the accepted range for electron-electron scattering, indicating the very weak presence of a single-magnon-scattering mechanism. We have tried to fit the low-temperature resistivity data by using the equation

$$\rho(T) = \rho_0 + \rho T^n. \tag{7}$$

From the fitting, we have found the value of $n = 2.2$, from which we can confirm that at low temperatures also there is a dominant magnon contribution, which is quite surprising and calls for further investigations of magnetic dynamics in this material. Previously, several authors have obtained different power (n) values depending on the temperature range considered. The value of n above 2 gives some signs of the weak-metallic character even at higher temperatures [12,48].

IV. CONCLUDING REMARKS

To summarize, we have synthesized a new Fe-based Heusler alloy Fe_2RuGe through the arc melting technique. The combined XRD, ND, and EXAFS study reveals that the material crystallizes in a disordered structure, which is also supported by the lower formation ground-state energy of the disordered structure over the ordered one, calculated by SQS+DFT. ^{57}Fe Mössbauer spectrometry confirms the inverse Heusler XA disorder with different sextets, strongly suggesting different Fe positions. From neutron diffraction, we confirm that the disorder between Fe and Ru in the 4c and 4d sites is 50:50 in nature. This leads to the mixing of Fe and Ru in the same plane. All these results validate that there are two different Fe environments compared to the Heusler structure. The compound exhibits a ferromagnetic to paramagnetic transition at a significantly high Curie temperature of 860 K and the saturation moment at 5 K is estimated to be 4.90 μ_B/f.u., which is much higher than the theoretically predicted S-P value of 4 μ_B/f.u.. The neutron diffraction experiments reveal that only Fe, distributed over different sites, contributes to the net magnetic moment while no moment could be detected on Ru site. Both theoretical calculation and the Mössbauer experiment support that there is a larger moment on Fe-4b site, in comparison with the other disordered Fe-(4c–4d) sites. This enhanced magnetic moment is explained by a large electronic charge transfer from Fe-4b to Ru, as calculated by DFT. The resistivity experiment confirms the presence of electron-electron behavior at the high-temperature range and a weak phonon contribution at low temperature compared to the magnon contribution.

ACKNOWLEDGMENTS

S.C. and S.G. would like to sincerely acknowledge UGC, India, and SINP, respectively, for the support of their fellowship. DFT calculations were performed using HPC resources from GENCI-CINES (Grant No. 2021-A0100906175). Work at the Ames National Laboratory (in part) was supported by the Department of Energy Basic Energy Sciences, Materials Sciences and Engineering Division, under Contract No. DEAC02-07CH11358.

[1] T. Graf, C. Felser, and S. S. Parkin, Simple rules for the understanding of Heusler compounds, Prog. Solid State Chem. **39**, 1 (2011).

[2] C. Felser and A. Hirohata, *Heusler alloys* (Springer, Berlin, 2015)

[3] S. Mondal, C. Mazumdar, R. Ranganathan, E. Alleno, P. C. Sreeparvathy, V. Kanchana, and G. Vaitheeswaran, Ferromagnetically correlated clusters in semimetallic Ru_2NbAl heusler alloy and its thermoelectric properties, Phys. Rev. B **98**, 205130 (2018).

[4] T. Gasi, V. Ksenofontov, J. Kiss, S. Chadov, A. K. Nayak, M. Nicklas, J. Winterlik, M. Schwall, P. Klaer, P. Adler, and C. Felser, Iron-based heusler compounds Fe_2YZ: Comparison with theoretical predictions of the crystal structure and magnetic properties, Phys. Rev. B **87**, 064411 (2013).

[5] Y. Du, G. Xu, X. Zhang, Z. Liu, S. Yu, E. Liu, W. Wang, and G. Wu, Crossover of magnetoresistance in the zero-gap half-metallic Heusler alloy Fe_2CoSi, Europhys. Lett. **103**, 37011 (2013).

[6] C. Fu, T. Zhu, Y. Liu, H. Xie, and X. Zhao, Band engineering of high performance p-type FeNbSb based half-heusler thermoelectric materials for figure of merit ZT> 1, Energy Environ. Sci. **8**, 216 (2015).

[7] N. S. Chauhan, P. R. Raghuvanshi, K. Tyagi, K. K. Johari, L. Tyagi, B. Gahtori, S. Bathula, A. Bhattacharya, S. D. Mahanti, V. N. Singh *et al.*, Defect engineering for enhancement of thermoelectric performance of (Zr, Hf)NiSn-based n-type half-Heusler alloys, J. Phys. Chem. C **124**, 8584 (2020).

[8] N. S. Chauhan, S. Bathula, B. Gahtori, S. D. Mahanti, A. Bhattacharya, A. Vishwakarma, R. Bhardwaj, V. N. Singh, and A. Dhar, Compositional tailoring for realizing high thermoelectric performance in Hafnium-free n-type ZrNiSn half-Heusler alloys, ACS Appl. Mater. Interfaces **11**, 47830 (2019).

[9] K. Özdoğan, E. Şaşıoğlu, and I. Galanakis, Engineering the electronic, magnetic, and gap-related properties of the quinternary half-metallic Heusler alloys, J. Appl. Phys. **103**, 023503 (2008).

[10] R. A. de Groot, F. M. Mueller, P. G. van Engen, and K. H. J. Buschow, New class of materials: half-metallic ferromagnets, Phys. Rev. Lett. **50**, 2024 (1983).

[11] S. Wurmehl, G. H. Fecher, H. C. Kandpal, V. Ksenofontov, C. Felser, H.-J. Lin, and J. Morais, Geometric, electronic, and magnetic structure of Co_2FeSi: Curie temperature and magnetic moment measurements and calculations, Phys. Rev. B **72**, 184434 (2005).

[12] S. Gupta, S. Chakraborty, S. Pakhira, C. Barreteau, J.-C. Crivello, B. Bandyopadhyay, J.-M. Greneche, E. Alleno, and C. Mazumdar, Coexisting structural disorder and robust spin-polarization in half-metallic FeMnVAl, Phys. Rev. B **106**, 115148 (2022).

[13] M. Siewert, M. E. Gruner, A. Hucht, H. C. Herper, A. Dannenberg, A. Chakrabarti, N. Singh, R. Arróyave, and P. Entel, A first-principles investigation of the compositional dependent properties of magnetic shape memory Heusler alloys, Adv. Eng. Mater. **14**, 530 (2012).

[14] H. D. Chopra, C. Ji, and V. V. Kokorin, Magnetic-field-induced twin boundary motion in magnetic shape-memory alloys, Phys. Rev. B **61**, R14913 (2000).

[15] H. Huang, X. Ma, Z. Liu, C. Zhao, S.-Q. Shi, and L. Chen, Simulation of multilevel cell spin transfer switching in a full-Heusler alloy spin-valve nanopillar, Appl. Phys. Lett. **102**, 042405 (2013).

[16] S. Zuo, F. Liang, Y. Zhang, L. Peng, J. Xiong, Y. Liu, R. Li, T. Zhao, J. Sun, F. Hu *et al.*, Zero-field skyrmions generated via premartensitic transition in $Ni_{50}Mn_{35.2}In_{14.8}$ alloy, Phys. Rev. Mater. **2**, 104408 (2018).

[17] B. Giri, A. I. Mallick, C. Singh, P. P. Madduri, F. Damay, A. Alam, and A. K. Nayak, Robust topological hall effect driven by tunable noncoplanar magnetic state in Mn-Pt-In inverse tetragonal Heusler alloys, Phys. Rev. B **102**, 014449 (2020).

[18] S. Ouardi, G. H. Fecher, C. Felser, and J. Kübler, Realization of spin gapless semiconductors: The Heusler compound Mn_2CoAl, Phys. Rev. Lett. **110**, 100401 (2013).

[19] L. Bainsla, A. I. Mallick, M. M. Raja, A. K. Nigam, B. S. D. C. S. Varaprasad, Y. K. Takahashi, A. Alam, K. G. Suresh, and K. Hono, Spin gapless semiconducting behavior in equiatomic quaternary CoFeMnSi Heusler alloy, Phys. Rev. B **91**, 104408 (2015).

[20] I. Žutić, J. Fabian, and S. D. Sarma, Spintronics: Fundamentals and applications, Rev. Mod. Phys. **76**, 323 (2004).

[21] N. D. Telling, P. S. Keatley, G. van der Laan, R. J. Hicken, E. Arenholz, Y. Sakuraba, M. Oogane, Y. Ando, and T. Miyazaki, Interfacial structure and half-metallic ferromagnetism in Co_2MnSi-based magnetic tunnel junctions, Phys. Rev. B **74**, 224439 (2006).

[22] M. A. McGuire, K. Shanavas, M. S. Kesler, and D. S. Parker, Tuning magnetocrystalline anisotropy by cobalt alloying in hexagonal Fe_3Ge1, Sci. Rep. **8**, 14206 (2018).

[23] R. Mahat, K. Shambhu, D. Wines, F. Ersan, S. Regmi, U. Karki, R. White, C. Ataca, P. Padhan, A. Gupta *et al.*, Tuneable structure and magnetic properties in $Fe_{3-x}V_xGe$ alloys, J. Alloys Compd. **830**, 154403 (2020).

[24] R. Mahat, K. Shambhu, D. Wines, S. Regmi, U. Karki, Z. Li, F. Ersan, J. Law, C. Ataca, V. Franco, A. Gupta, and P. LeClair, Influence of Cr-substitution on the structural, magnetic, electron transport, and mechanical properties of $Fe_{3-x}Cr_xGe$ Heusler alloys, J. Magn. Magn. Mater. **521**, 167398 (2021).

[25] S. Keshavarz II, N. Naghibolashrafi, M. E. Jamer, K. Vinson, D. Mazumdar, C. L. Dennis, W. Ratcliff II, J. A. Borchers, A. Gupta, and P. LeClair, Fe_2MnGe: A hexagonal heusler analogue, J. Alloys Compd. **771**, 793 (2019).

[26] J. Rodríguez-Carvajal, Recent advances in magnetic structure determination by neutron powder diffraction, Phys. B: Condens. Matter **192**, 55 (1993).

[27] B. Ravel and M. Newville, Athena, artemis, hephaestus: data analysis for x-ray absorption spectroscopy using Ifeffit, J. Synchrotron Radiat. **12**, 537 (2005).

[28] M. Avdeev and J. R. Hester, Echidna: a decade of high-resolution neutron powder diffraction at opal, J. Appl. Crystallogr. **51**, 1597 (2018).

[29] P. E. Blöchl, Projector augmented-wave method, Phys. Rev. B **50**, 17953 (1994).

[30] G. Kresse and J. Hafner, Ab initio molecular-dynamics simulation of the liquid-metal–amorphous-semiconductor transition in germanium, Phys. Rev. B **49**, 14251 (1994).

[31] G. Kresse and J. Hafner, Norm-conserving and ultrasoft pseudopotentials for first-row and transition elements, J. Phys.: Condens. Matter **6**, 8245 (1994).

[32] J. P. Perdew, K. Burke, and M. Ernzerhof, Generalized gradient approximation made simple, Phys. Rev. Lett. **77**, 3865 (1996).

[33] P. E. Blöchl, O. Jepsen, and O. K. Andersen, Improved tetrahedron method for brillouin-zone integrations, Phys. Rev. B **49**, 16223 (1994).

[34] A. Zunger, S.-H. Wei, L. G. Ferreira, and J. E. Bernard, Special quasirandom structures, Phys. Rev. Lett. **65**, 353 (1990).

[35] J. M. Sanchez, F. Ducastelle, and D. Gratias, Generalized cluster description of multicomponent systems, Physica A **128**, 334 (1984).

[36] A. van de Walle, P. Tiwary, M. De Jong, D. Olmsted, M. Asta, A. Dick, D. Shin, Y. Wang, L.-Q. Chen, and Z.-K. Liu, Efficient stochastic generation of special quasirandom structures, Calphad **42**, 13 (2013).

[37] A. van de Walle, Multicomponent multisublattice alloys, nonconfigurational entropy and other additions to the alloy theoretic automated toolkit, Calphad **33**, 266 (2009).

[38] S. Chakraborty, S. Gupta, S. Pakhira, A. Biswas, Y. Mudryk, R. Choudhary, A. Kumar, A. Das, and C. Mazumdar, Origin of magnetic ordering in half-Heusler RuMnGa, Phys. Rev. B **108**, 054430 (2023).

[39] T. Jeong, Electronic structure and magnetism of $FeGe_2$, Solid State Commun. **141**, 329 (2007).

[40] F. Varret, J. Greneche, and J. Teillet, *Proceedings of the International Workshop Mössbauer Spectroscopy* (Springer Science & Business Media, Berlin, 1983), p. 101.

[41] S. J. Campbell and F. Aubertin, *Mössbauer Spectroscopy Applied to Inorganic Chemistry*, edited by G. J. Long and F. Grandjean (Plenum Press, New York, 1989), p. 183-242.

[42] S. Mishra, D. Rambabu, A. Grover, R. Pillay, P. Tandon, H. Devare, and R. Vijayaraghavan, Do ruthenium atoms possess local moment in the magnetically ordered system $Fe_{3-x}Ru_xSi$? Solid State Commun. **53**, 321 (1985).

[43] G. Cao, S. McCall, M. Shepard, J. E. Crow, and R. P. Guertin, Thermal, magnetic, and transport properties of single-crystal $Sr_{1-x}Ca_xRuO_3$ ($0 < x < 1.0$), Phys. Rev. B **56**, 321 (1997).

[44] S. Dubiel, Relationship between the magnetic hyperfine field and the magnetic moment, J. Alloys Compd. **488**, 18 (2009).

[45] J. Drijver, S. Sinnema, and F. Van der Woude, Magnetic properties of hexagonal and cubic Fe_3Ge, J. Phys. F **6**, 2165 (1976).

[46] A. K. Arzhnikov, L. V. Dobysheva, G. N. Konygin, E. V. Voronina, and E. P. Yelsukov, Hyperfine magnetic fields in partially disordered Fe-Si alloys with Si content near 25 at.%, Phys. Rev. B **65**, 024419 (2001).

[47] J. Bœuf, C. Pfleiderer, and A. Faißt, Low-temperature properties of the semi-Heusler compound CuMnSb, Phys. Rev. B **74**, 024428 (2006).

[48] J. Nag, D. Rani, D. Singh, R. Venkatesh, B. Sahni, A. K. Yadav, S. N. Jha, D. Bhattacharyya, P. D. Babu, K. G. Suresh, and A. Alam, CoFeVSb: A promising candidate for spin valve and thermoelectric applications, Phys. Rev. B **105**, 144409 (2022).

[49] P. L. Rossiter, *The Electrical Resistivity of Metals and Alloys*, Vol. 6 (Cambridge University Press, Cambridge, 1991).